Monthly Notices of the ROYAL ASTRONOMICAL SOCIETY

MNRAS **464,** 4624–4640 (2017) doi:10.1093/mnras/stw2608
Advance Access publication 2016 October 12

GRB 110715A: the peculiar multiwavelength evolution of the first afterglow detected by ALMA

R. Sánchez-Ramírez,[1,2,3★] P. J. Hancock,[4,5] G. Jóhannesson,[6] Tara Murphy,[4] A. de Ugarte Postigo,[1,7] J. Gorosabel,[1,2,3†] D. A. Kann,[8,9] T. Krühler,[9,10] S. R. Oates,[1,11] J. Japelj,[12] C. C. Thöne,[1] A. Lundgren, D. A. Perley,[7] D. Malesani,[7] I. de Gregorio Monsalvo,[10,13] A. J. Castro-Tirado,[1] V. D'Elia,[14,15] J. P. U. Fynbo,[7] D. Garcia-Appadoo,[10,13] P. Goldoni,[16] J. Greiner,[9,17] Y.-D. Hu,[1] M. Jelínek,[1,18] S. Jeong,[1,19] A. Kamble,[20] S. Klose,[8] N. P. M. Kuin,[11] A. Llorente,[21] S. Martín,[10,13] A. Nicuesa Guelbenzu,[8] A. Rossi,[22] P. Schady,[9] M. Sparre,[7] V. Sudilovsky,[23] J. C. Tello,[1] A. Updike,[24] K. Wiersema[25] and B.-B. Zhang[1,26]

Affiliations are listed at the end of the paper

Accepted 2016 October 6. Received 2016 October 6; in original form 2016 April 1

ABSTRACT

We present the extensive follow-up campaign on the afterglow of GRB 110715A at 17 different wavelengths, from X-ray to radio bands, starting 81 s after the burst and extending up to 74 d later. We performed for the first time a GRB afterglow observation with the ALMA observatory. We find that the afterglow of GRB 110715A is very bright at optical and radio wavelengths. We use the optical and near-infrared spectroscopy to provide further information about the progenitor's environment and its host galaxy. The spectrum shows weak absorption features at a redshift $z = 0.8225$, which reveal a host-galaxy environment with low ionization, column density, and dynamical activity. Late deep imaging shows a very faint galaxy, consistent with the spectroscopic results. The broad-band afterglow emission is modelled with synchrotron radiation using a numerical algorithm and we determine the best-fitting parameters using Bayesian inference in order to constrain the physical parameters of the jet and the medium in which the relativistic shock propagates. We fitted our data with a variety of models, including different density profiles and energy injections. Although the general behaviour can be roughly described by these models, none of them are able to fully explain all data points simultaneously. GRB 110715A shows the complexity of reproducing extensive multiwavelength broad-band afterglow observations, and the need of good sampling in wavelength and time and more complex models to accurately constrain the physics of GRB afterglows.

Key words: radiation mechanisms: non-thermal – relativistic processes – gamma-ray burst: individual: GRB 110715A – ISM: abundances – ISM: jets and outflows.

1 INTRODUCTION

Gamma-ray bursts (GRBs; Klebesadel, Strong & Olson 1973) are the most violent explosions in the Universe. They are characterized by a short flash of gamma-ray photons followed by a long-lasting afterglow that can be observed at all wavelengths. They can be classified into two types based on the duration (and the hardness) of their γ-emission: short and long GRBs ($T_{90} < 2$ s (hard spectrum) and $T_{90} > 2$ s (soft spectrum), respectively; Kouveliotou et al. 1993). Currently, the most favoured model to explain the origin of GRBs is a highly magnetized relativistic jet, but more prompt polarimetric observations are needed in order to confirm this (Mundell et al. 2013; Kopač et al. 2015). The prompt emission likely originates from either internal shocks in the photosphere of the jet or magnetic dissipation in a magnetically dominated jet (see Zhang & Yan 2011; Zheng et al. 2012, and references therein). The afterglow emission, however, is thought to originate from external shocks caused by the jet's interaction with the interstellar medium (ISM). Multiwavelength emission is expected to be produced by a forward shock moving into the ISM and a reverse shock (RS) moving into

★ E-mail: ruben@iaa.es
† Deceased.

the expanding jet (Mészáros & Rees 1993; Sari, Piran & Narayan 1998; Sari, Piran & Halpern 1999). The RS is supposed to be short lived, with most of the afterglow emission being generated by the forward shock.

The electrons accelerated at the shock fronts emit synchrotron radiation as they interact with the magnetic field behind the shock fronts. By modelling this emission, we can determine the physical parameters of the GRB ejecta and the structure of the ISM near the progenitor along the line of sight to Earth. The most popular way to extract the parameters is by using an analytical model for the expected shape of the afterglow light curves and spectrum (Rhoads 1997; Sari et al. 1998; Wijers & Galama 1999). The emission is split into regions in time and wavelength, where the resulting light curve and spectrum can be approximated by power laws. The slopes of these segments along with the location of the spectral breaks are then used to determine the physical parameters. An alternative method is to model the emission using a numerical code that takes as input the physical parameters of interest (Panaitescu & Kumar 2002; Jóhannesson, Björnsson & Gudmundsson 2006). In addition to requiring fewer approximations, the numerical models allow us to study a more complex structure for the ISM and the GRB ejecta and is therefore our method of choice for this study.

To properly determine the physical properties of the GRB ejecta, a wide range of accurate multiwavelength observations are needed with as good time coverage as possible. The millimetre/submillimetre range is of crucial importance in constraining the afterglow models as it is where the flux density of the emission peaks during the first few days after the GRB onset. In this range, the capabilities of the new Atacama Large Millimeter Array (ALMA) observatory bring an important leap forward, thanks to its great improvement in resolution and sensitivity in comparison with previous observatories (de Ugarte Postigo et al. 2012a).

It is widely accepted that long GRBs are created by the explosive death of massive stars (Hjorth et al. 2003; Woosley & Bloom 2006), probably rapidly rotating Wolf-Rayets (for a review see e.g. Crowther 2007). However, it remains unclear what the specific mechanism in the core-collapse process is that triggers the formation of a jet. Given the short life periods of such massive stars and their luminosity, GRB afterglows can be used as powerful tracers of star-forming galaxies over a wide range of redshifts (e.g. Kistler et al. 2009; Robertson & Ellis 2012; Krühler et al. 2015; Schulze et al. 2015; Vergani et al. 2015). To date, spectroscopically confirmed GRB redshifts range from $z = 0.0085$ (GRB 980425A; Tinney et al. 1998; Galama et al. 1998) to $z = 8.2$ (GRB 090423A; Salvaterra et al. 2009; Tanvir et al. 2009), and photometric redshifts have been proposed up to $z = 9.4$ (GRB 090429B; Cucchiara et al. 2011).

Optical/Near InfraRed (NIR) spectroscopy of GRB afterglows can also be used to study the intervening matter present along the line of sight at different distance scales, ranging from regions around the progenitor to distant intervening galaxies. Its strength resides in the extremely bright afterglow, making it possible to measure atomic/molecular transitions in the host galaxy and intervening systems (e.g. D'Elia et al. 2014), even when the probed galaxies are not detected by deep direct imaging. It made possible to accurately probe absorption metalliticity out to $z \geq 5$ (e.g. Sparre et al. 2014; Hartoog et al. 2015).

In this paper, we present observations of the afterglow and host galaxy of GRB 110715A, aiming at understanding the physical processes involved in the explosion and the environment in which it occurred. Our data include radio, submillimetre, near-infrared, optical, ultraviolet, and X-ray observations. In Section 2, we introduce the observations available for this event, in Section 3, we explain the results of these observations and discuss the implications, and in Section 4, we present our conclusions.

2 OBSERVATIONS

2.1 Gamma-ray emission

The *Swift* (Gehrels et al. 2004) Burst Alert Telescope (BAT; Barthelmy et al. 2005) triggered and located GRB 110715A on 2011 July 15 at T_0= 13:13:50 UT (Sonbas et al. 2011). The gamma-ray light curve shows a double-peaked structure with a duration of T_{90}= 13.0 ± 4.0 s (90 per cent confidence level) in the observer frame. Therefore, we classify GRB 110715A as a long burst.

Analysis of the time-integrated spectrum from *Konus-Wind* gave the best fit as a Band function with the following parameters: $\alpha_1 = -1.23^{+0.09}_{-0.08}$, $\alpha_2 = -2.7^{+0.2}_{-0.5}$, $E_p = 120^{+12}_{-11}$ (Golenetskii et al. 2011). GRB 110715A was also detected by *INTEGRAL*/SPI-ACS and *Suzaku*/WAM [see more details in (Golenetskii et al. 2011) and (Sonbas et al. 2011)].

2.2 X-ray afterglow observations

The X-Ray Telescope (XRT; Burrows et al. 2005) onboard *Swift* began observing the field 90.9 s after the BAT trigger, localizing the X-ray afterglow at RA(J2000) = $15^h50^m44.00^s$, Dec.(J2000) = $-46^\circ14'\,07''.5$ with an uncertainty of $1''.4$ (90 per cent confidence level; Evans et al. 2011).

The unabsorbed X-ray afterglow light curve used in this paper has been extracted from the BURST ANALYZER[1] (Evans et al. 2007, 2009, 2010), which uses the spectral slope to derive the flux densities at an energy of 2 keV and assumes a hydrogen column density N(H) = $1.6^{+0.5}_{-0.4} \times 10^{22}$ cm^{-2}. These observations are shown in Fig. 1 and tabulated in Table 1.

2.3 UV/Optical/NIR afterglow observations

GRB 110715A was followed up in UV/Optical/NIR wavelengths with *Swift* (+UVOT) and the 2.2 m MPG telescope (+GROND). Light curves are shown in Fig. 1 and tabulated in Table 1 as well.

This burst had a very bright optical counterpart in spite of the high Galactic extinction caused by its location close to the Galactic plane (Evans et al. 2011). The GRB afterglow study was affected by the Galactic reddening, initially estimated to be $E(B - V) = 0.59$ mag according to the dust maps of Schlegel, Finkbeiner & Davis (1998), and later $E(B - V) = 0.52$ mag following Schlafly & Finkbeiner (2011). We adopted the latest value. Computed effective wavelengths and extinction for each band are presented in Table 2.

2.3.1 UVOT imaging

The *Swift* Ultra-Violet/Optical Telescope (UVOT; Roming et al. 2005) began settled observations of the field of GRB 110715A 100 s after the trigger (Breeveld et al. 2011). The afterglow was detected in the *white*, *u*, *b*, and *v* filters at RA(J2000) = $15^h50^m44.09^s$, Dec.(J2000) = $-46^\circ14'\,06''.5$, with a 2σ uncertainty of about $0''.62$. For this analysis, we have reduced both image and event-mode data grouped with binning $\Delta t/t \sim 0.2$. Before the count rates were extracted from the event lists, the astrometry was refined following

[1] http://www.swift.ac.uk/burst_analyser

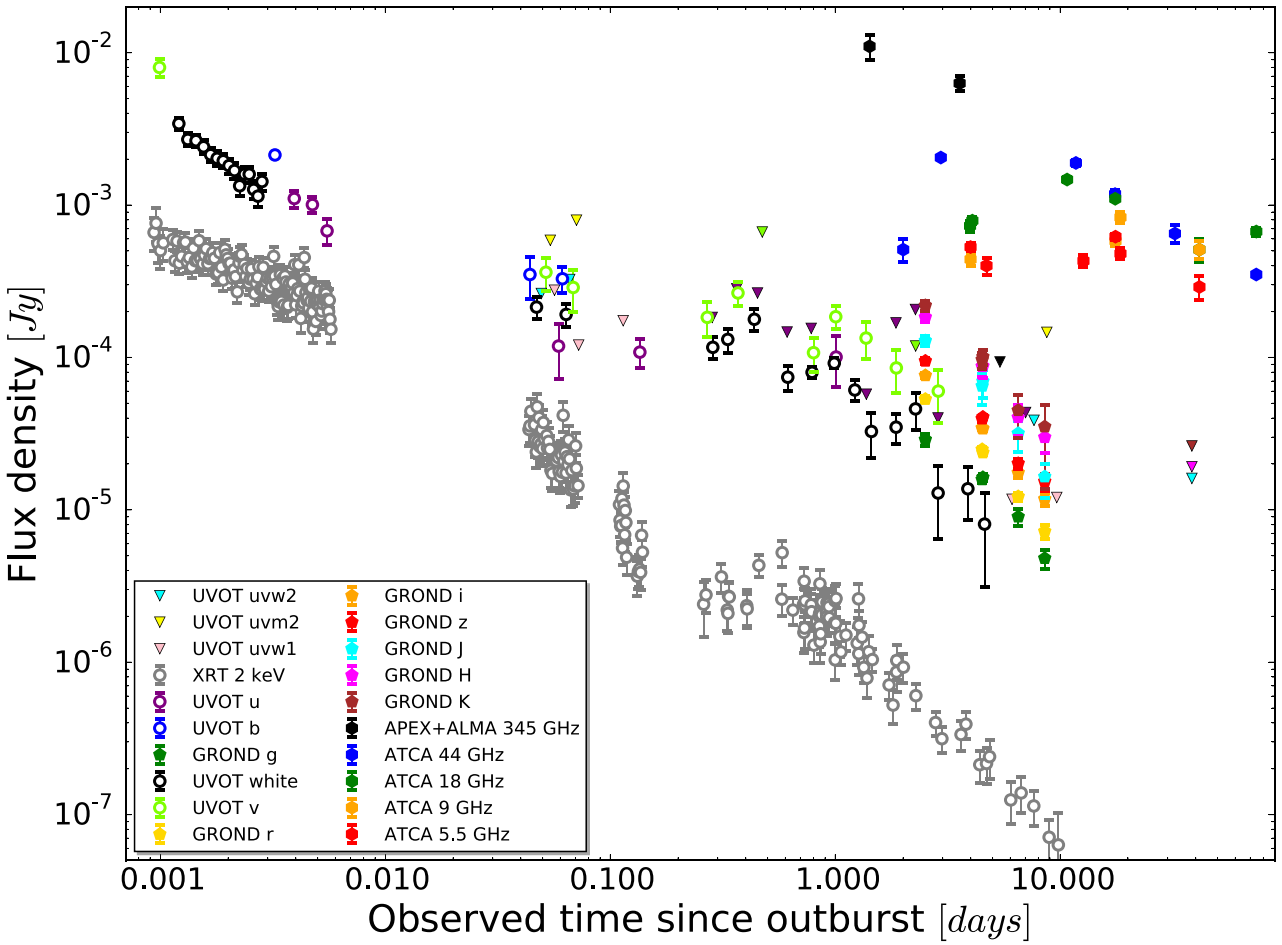

Figure 1. Afterglow light curve (Galactic extinction corrected) of the 17 bands observed. Upper limits are denoted by down-pointing triangles.

Table 1. Broad band multiwavelength observations of GRB 110715A. The full table is available in the online version.

$T - T_0$ (days)	Flux (Jy)	AB (mag)	Band
0.000 94	$(1.32 \pm 0.33) \times 10^{-04}$	$18.60^{+0.24}_{-0.31}$	XRT 2 keV
0.000 96	$(1.52 \pm 0.37) \times 10^{-04}$	$18.44^{+0.24}_{-0.31}$	XRT 2 keV
0.000 98	$(1.12 \pm 0.27) \times 10^{-04}$	$18.78^{+0.24}_{-0.31}$	XRT 2 keV
0.001 00	$(1.01 \pm 0.25) \times 10^{-04}$	$18.89^{+0.24}_{-0.31}$	XRT 2 keV
0.001 03	$(1.13 \pm 0.26) \times 10^{-04}$	$18.77^{+0.23}_{-0.29}$	XRT 2 keV
0.001 14	$(1.19 \pm 0.17) \times 10^{-04}$	$18.71^{+0.15}_{-0.17}$	XRT 2 keV
0.001 16	$(0.86 \pm 0.13) \times 10^{-04}$	$19.06^{+0.16}_{-0.18}$	XRT 2 keV
0.001 19	$(1.16 \pm 0.17) \times 10^{-04}$	$18.74^{+0.15}_{-0.18}$	XRT 2 keV
...	...	...	...

Table 2. Effective wavelengths and extinction coefficients.

Band	$\lambda_{\rm eff}$ (μm)	$A_\lambda{}^a$
UVOT uvw2	0.193	4.099
UVOT uvm2	0.225	4.582
UVOT uvw1	0.260	3.623
UVOT u	0.351	2.587
UVOT b	0.441	2.021
GROND g'	0.459	2.018
UVOT *white*	0.483	2.566
UVOT v	0.545	1.628
GROND r'	0.622	1.393
GROND i'	0.764	1.042
FORS2 Ic	0.786	0.949
GROND z'	0.899	0.775
GROND *J*	1.239	0.455
GROND *H*	1.646	0.291
GROND *K*	2.170	0.187

Note. [a]$E(B-V) = 0.52$ mag (Schlafly & Finkbeiner 2011).

the methodology of Oates et al. (2009). The photometry was then extracted from the event lists and image files based on the FTOOLS *uvotevtlc* and *uvotmaghist*, respectively, using a source aperture centred on the optical position and a background region located in a source-free zone. We used a 3 arcsec source aperture to avoid contamination from neighbouring stars and applied aperture corrections to the photometry in order to be compatible with the UVOT calibration (Breeveld et al. 2011). The analysis pipeline used the software HEADAS 6.10 and the UVOT calibration 20111031.

2.3.2 *GROND imaging*

We obtained the follow-up observations of the optical/NIR afterglow of GRB 110715A with the seven-channel imager GROND (GRB optical/near-infrared detector; Greiner et al. 2008) mounted on the 2.2 m MPG@ESO telescope stationed in La Silla, Chile. The first observations were obtained 2.5 d after the trigger, after losing the first two nights due to weather. This first epoch suffers

from very bad seeing, 1.″5 – 1.″9 depending on the band, but the optical/NIR afterglow was clearly detected (Updike et al. 2011). Deeper follow-up under better conditions in three further epochs reveals a faint nearby source which exhibits a stellar Point Spread Function (PSF). The presence of this source was carefully accounted for during the data analysis. The GROND optical and NIR image reduction and photometry were performed by calling on standard IRAF tasks (Tody 1993) using the custom GROND pipeline (Yoldaş et al. 2008), similar to the procedure described in Krühler et al. (2008). Hereby, we used SEXTRACTOR (Bertin & Arnouts 1996) for background modelling, and bright sources were masked out, which yields improved results in the case of this crowded field. A late epoch was obtained 38 d after the GRB which was supposed to be used for image subtraction purposes, but a positioning error led to the afterglow position being covered only in the NIR frames.

Afterglow magnitudes in the optical were measured against comparison stars calibrated to the SDSS catalogue (Aihara et al. 2011), obtained from observing an SDSS field at similar airmass immediately after the fourth epoch, in photometric conditions. NIR magnitudes were measured against on-chip comparison stars taken from the 2MASS catalogue (Skrutskie et al. 2006). The results of the photometry are displayed in Table 1.

2.4 Submillimetre afterglow observations

The Atacama pathfinder experiment telescope (APEX) observations began on July 16, 1.42 d after the burst and were performed in the 345 GHz band using the photometric mode of the Large Apex BOlometer CAmera (LABOCA; Siringo et al. 2009) under good weather conditions. Data reduction was done using the BOA (1), CRUSH, and MINICRUSH (Kovács 2008) software packages. Using these observations, we discovered a bright submillimetre counterpart at 10.4 ± 2.4 mJy (de Ugarte Postigo et al. 2011).

As a test of the target of opportunity programme, GRB 110715A was also observed with the ALMA, yielding a detection with a flux density of 4.9 ± 0.6 mJy at 345 GHz (de Ugarte Postigo et al. 2012a). The ALMA observations began on July 19 at 02:50 UT (3.57 d after the burst), and they were carried out making use of only seven antennas during 25 min on source. We present the data in Fig. 2.

In spite of being obtained during a test observation, with almost an order of magnitude fewer antennas than are available with the full observatory, this was the deepest observation carried out to date

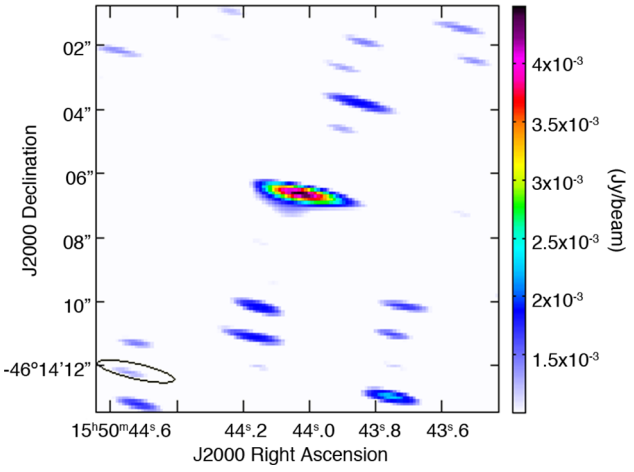

Figure 2. ALMA image at 345 GHz. The beam size (0.″3 × 0.″1, P.A. = 76°) is shown in the lower left corner.

at 345 GHz of a GRB afterglow (de Ugarte Postigo et al. 2012a). The ALMA observation also provides the most accurate coordinates available for this GRB. The centroid of the afterglow is located at RA(J2000) = $15^{h}50^{m}44.05^{s}$ and Dec.(J2000) = −46° 14′ 06.″5 with a synthesized beam size of 0.″3 × 0.″1 at a position angle of 76°, which provides an astrometric accuracy $\lesssim$0.″02. The differences between the optical and radio reference frames only limit this precision to be $\lesssim$0.″05 (e.g. Johnston & de Vegt 1986).

2.5 Radio afterglow observations

Following the detection of an afterglow at submillimetre wavelengths with APEX (de Ugarte Postigo et al. 2011), radio observations were obtained with the Australia Telescope Compact Array (ATCA; Wilson et al. 2011) two and three days after the trigger. These observations resulted in further detections of the afterglow at 44 GHz (Hancock, Murphy & Schmidt 2011). This GRB was monitored at 44, 18, 9, and 5 GHz for up to 75 d post-burst, where the flux remained at a sub-mJy level. The lower frequency observations were complicated by the presence of a second source within the field of view (MGPS J155058-461105). The data were reduced using standard procedures in MIRIAD (Sault, Teuben & Wright 1995). An additional late-time visit was performed on 2013 August 12 at 5.5 and 9 GHz, to understand the possible contribution of the host galaxy, which was found to be negligible at both bands. The flux evolution of the afterglow at the four ATCA frequencies is also shown in Fig. 1 and tabulated in Table 1, together with the rest of the observing bands.

2.6 Optical/nIR afterglow spectra

VLT/X-shooter (Vernet et al. 2011), an optical/nIR intermediate resolution spectrograph mounted at the Very Large Telescope (VLT) Unit Telescope (UT) 2 in Paranal Observatory (Chile), was used to observe the GRB afterglow starting 12.7 hr after the *Swift* trigger. The seeing was 0.″9, but observations had to be interrupted due to wind constraints (Piranomonte et al. 2011). The observing log is shown in Table 3. We processed the spectra using version 2.0.0 of the X-shooter data reduction pipeline (Goldoni et al. 2006; Modigliani et al. 2010). As the observations were stopped after one exposure, the standard nodding reduction could not be performed. We thus reduced the single frames of each arm with the following steps: we performed bias subtraction, cosmic ray detection and subtraction (van Dokkum 2001), and flat-field division on the raw frames. From these processed frames, the sky emission was subtracted using the Kelson (2003) method and 1D spectra were extracted directly order by order from the sky-subtracted and flat-field divided frame using optimal extraction (Horne 1986). The resulting spectra were merged weighting them by the errors and the final merged spectra were then averaged in IDL. The spectra were flux calibrated using observations of the standard star LTT7987 taken the same night. The complete X-shooter spectrum is shown in Fig. 3.

Table 3. X-shooter observations log.

Mean $T-T_0$ (hr)	Arm	Exp. time (s)	Slit width (arcsec)	Resolution[a]
12.60	UVB	618.02	1.0	4350
12.60	VIS	612.04	0.9	7450
12.60	NIR	600.00	0.9[b]	5300

Notes. [a]Nominal values. [b]*K*-band blocker was not used.

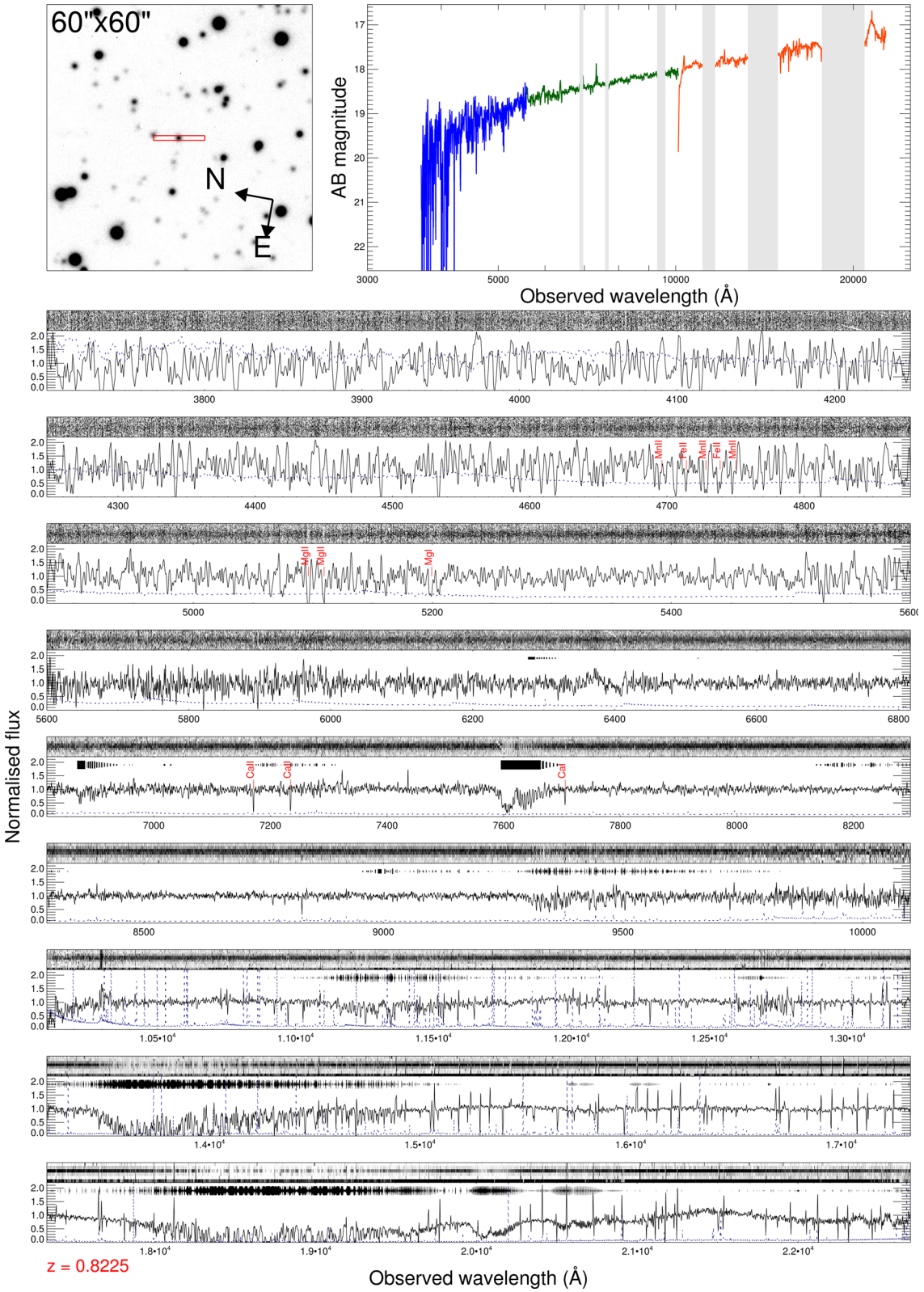

Figure 3. X-shooter spectra. Upper panels are the finding chart (left) and an overview of the complete flux calibrated spectra, corrected for Galactic extinction (right). In the bottom plot, we show the normalized spectra, with three panels per arm, starting at top with UVB and followed by VIS and NIR. Each panel includes the 2D image and 1D signal and error spectrum. Telluric absorptions are indicated by black bands above the 1D spectrum, their thickness is a measure of the absorption strength.

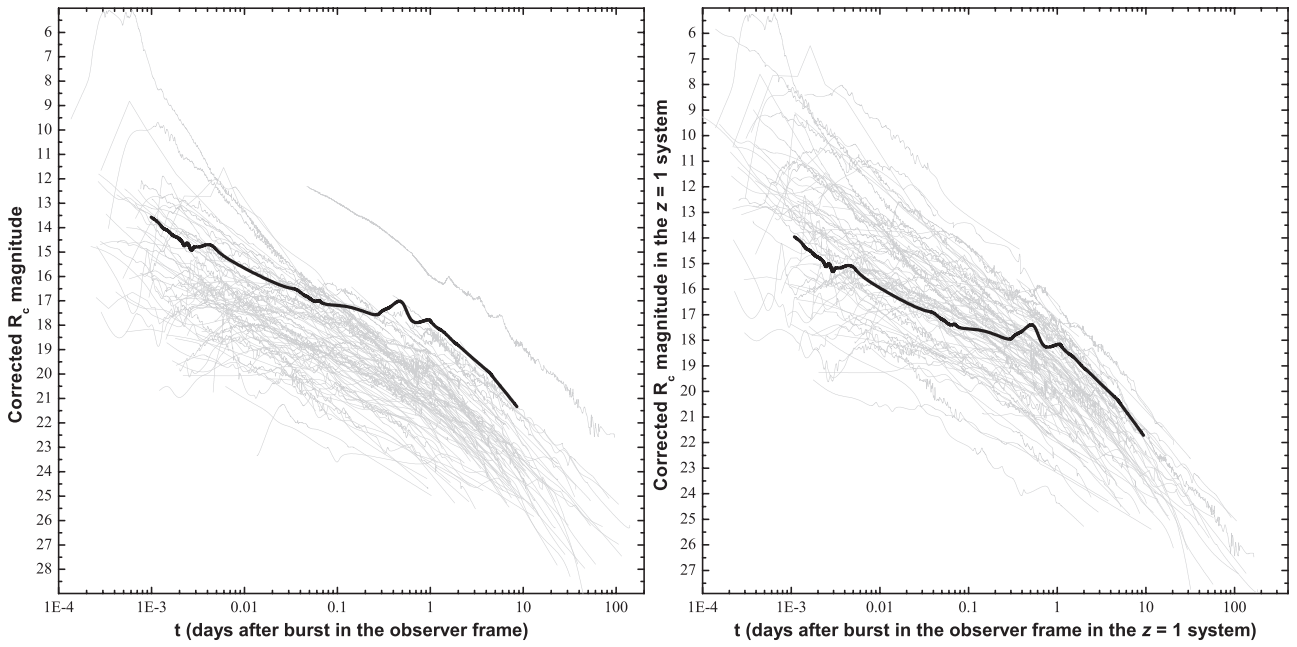

Figure 4. The observed R_C-band afterglow of GRB 110715A in comparison to a large sample of long GRB afterglows (left). After correction for the significant foreground extinction, it is seen to be one of the brightest afterglows ever observed. After correcting for rest-frame extinction and shifting to $z = 1$ (right), the afterglow of GRB 110715A is more common, although it remains among the more luminous detected to date at late times.

2.7 Host-galaxy imaging

606 d after the burst, the field of GRB 110715A was revisited using GROND searching for a possible host-galaxy contribution. However, the data did not reveal any underlying source. We therefore derive only detection limits.

A deeper exposure was obtained in 2013 August with FORS2 at ESO's VLT 751 d after the burst. The observation consisted of 10×240 s in I_C-band, with a seeing of $0\farcs55$, and data were reduced in a similar fashion as the GROND imaging. An object is detected close to the afterglow position at a magnitude of 26.40 ± 0.36 mag.

3 RESULTS AND DISCUSSION

3.1 The afterglow of GRB 110715A in a global context

Using the UVOT and GROND data, and adding the early R_C band observations from Nelson (2011), we construct a composite light curve by shifting all data to the R_C band (no evidence for chromatic evolution is found). This light curve extends over almost four decades in time. Comparing it to the sample of long GRB afterglow light curves taken from Kann, Klose & Zeh (2006), and Kann et al. (2010, 2011), we find that (after correcting for the significant – 1.6 mag – foreground extinction) the afterglow is among the brightest ever detected (especially after ∼0.3 d, see Fig. 4 left-hand panel), comparable to those of GRB 991208 (Castro-Tirado et al. 2001) and GRB 060729 (Cano et al. 2011), both at lower redshift (see Section 3.2). It becomes fainter than 20th magnitude only after about 4.5 d. Using the GROND data, we find a best fit for the spectral energy distribution (SED) of the afterglow with $\beta = 0.90 \pm 0.22$, and a small (essentially zero) $A_V = 0.09 \pm 0.18$ using SMC dust. With these data and knowledge of the redshift, we use the method of Kann et al. (2006) to shift the afterglow, corrected for all extinction, to $z = 1$. We find a magnitude shift of $\mathrm{d}Rc = +0.38^{+0.17}_{-0.32}$. At one day after the trigger (in the $z = 1$ frame), it is $R_C = 17.97^{+0.19}_{-0.33}$, and $R_C = 13.90^{+0.23}_{-0.35}$ at 0.001 d. This places the afterglow into the tight peak found by Kann et al. (2010) (their fig. 6), which is formed by afterglows which are likely forward-shock dominated at early times already. This does not mean that a RS component is not present. According to Kann et al. (2010), the early afterglow can be classified as 'Limit + Slow Decay' (Kann et al. 2010, their table 5). In this sense, except for the rebrightenings, the afterglow is seen to be typical.

In Fig. 5, we compare the radio and submillimetre emission of GRB 110715A to the samples of de Ugarte Postigo et al. (2012a) and Chandra & Frail (2012): in submillimetre, the afterglow peak brightness is among the brightest observed, with similar luminosity as GRB 030329, GRB 100621A, or GRB 100418A, but still an order of magnitude less luminous than the highest luminosity events (GRB 980329, GRB 090313, GRB 080129, or GRB 050904). The situation in radio is similar, with GRB 110715A being amongst the brightest events.

At early times, the physical size of the GRB afterglow emission region will be small, and thus there is the possibility of interstellar scintillation (ISS) modulating the observed flux of the afterglow, as has been seen previous in GRBs such as GRB 970508 (Frail et al. 1997). GRB 970508 was seen to have large (40–50 per cent) fractional modulations in flux at 1.4 and 8.6 GHz for up to two months post burst, after which the intrinsic source size became large enough to break the conditions under which ISS is possible.

According to Walker (1998), the transition frequency at the location of GRB 110715A is ∼40 GHz, indicating that, when present, scintillation should be strong ($m_d > 1$) below this frequency, and weak ($m_d < 1$) at higher frequencies. The temporal resolution of our observations during the first two weeks after the GRB is low so we are unable to measure scintillation. However, differences between the modelled and observed flux densities seen at $\lesssim$40 GHz in the first two weeks post burst are consistent with scintillation.

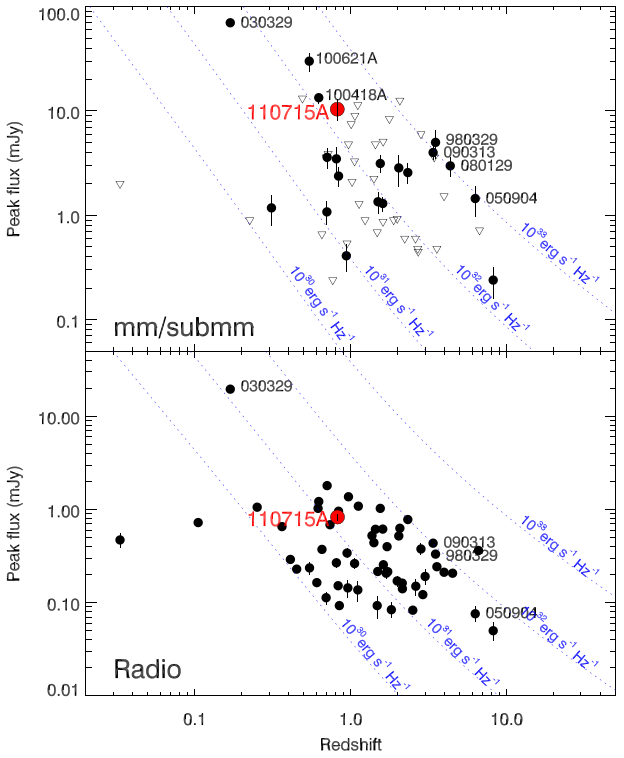

Figure 5. Top: millimetre/submillimetre afterglow as compared with the sample of de Ugarte Postigo et al. (2012a). Bottom: radio afterglow of GRB 110715A compared with the sample of Chandra & Frail (2012).

3.2 Spectral absorption lines of the optical afterglow

We detect eight absorption features in the complete X-shooter spectrum that we identify as caused by Fe II, Mg II, Mg I, Ca II, and Ca I at a common redshift of 0.8225 ± 0.0001. For recent Planck cosmological parameters ($\Omega_M = 0.315$, $\Omega_\Lambda = 0.685$, $H_0 = 67.3$ km s^{-1} Mpc^{-1}; Planck Collaboration 2014), this redshift corresponds to a luminosity distance of 5357.86 Mpc.

We have measured the equivalent widths of these lines and limits for several others using the self-developed code used in Fynbo et al. (2009) and de Ugarte Postigo et al. (2012b). The results are shown in Table 4, as well as the composite afterglow spectrum by Christensen et al. (2011) for comparison purposes. Using the prescriptions given by de Ugarte Postigo et al. (2012b), we find that the neutral element population is higher than average (see Fig. 6). Detection of Ca Iλ4227, a line rarely observed in GRB afterglows (de Ugarte Postigo et al. 2012b), also supports the low-ionization hypothesis of the material in the line of sight to GRB 110715A.

Following the prescription of de Ugarte Postigo et al. (2012b), we obtain a line strength parameter for GRB 110715A of LSP = −0.83 ± 0.47, implying that this event is in the percentile 13.4 of line strengths, and indicating a lower than average column density of material in the line of sight (86.6 per cent of GRBs have stronger lines). This often indicates a small host galaxy (de Ugarte Postigo et al. 2012b). This is consistent with the fact that there are no velocity components in the absorption features faster than 30 km s^{-1}.

3.3 The host galaxy

We computed the distance between the afterglow and the host-galaxy core (see Fig. 7). The centroid is offset by 0.21 ± 0.03 arcsec with respect to the ALMA position, which at the redshift of GRB 110715A corresponds to 1.56 ± 0.19 kpc. This is comparable to the typical offset of 1.2 kpc seen for long GRBs (Bloom, Kulkarni & Djorgovski 2002; de Ugarte Postigo et al. 2012b). The host absolute magnitude (AB) would be $M = -18.2$ mag at a rest-frame wavelength of 4200 Å, which is similar to the Johnson B-band (without needing to make assumptions on the host-galaxy spectral index).

The luminosity of the host galaxy is low, even relative to other GRB hosts (which tend to occur in lower mass and lower luminosity galaxies than average at $z \lesssim 1.5$; e.g. Perley et al. 2016a), although it is by no means extreme or exceptional. For example, relative to the UV luminosity distribution of nine galaxies at roughly similar redshift ($0.5 < z < 1.1$) in the TOUGH sample (Schulze et al. 2015), this host galaxy is less luminous than six or more, depending on the unknown k-correction across the Balmer break which is not known for the TOUGH sample. We also compared this magnitude to synthetic B-band magnitudes of galaxies from the larger, multicolour SHOALS sample (Perley et al. 2016b, and work in preparation). The host of GRB 110715A is about 0.6 mag less luminous than the median B magnitude of $0.5 < z < 1.1$ galaxies in this sample and is more luminous than only five out of these 21 galaxies. Compared to a more local galaxy population, it is slightly more luminous than the LMC ($M_B \sim -17.5$) but of course much less luminous than nearby spirals such as the Milky Way or M31 ($M_B \sim -20.5$ to -21). This faint host galaxy is consistent with the faint and unresolved absorption features seen in the afterglow spectrum. Considering also its very low ionization environment, all evidence suggest that the sight-line towards GRB 110715A is probing a small dwarf host galaxy, maybe in its initial star-forming episode due to the low background ionizing radiation, which keeps an unusual abundance of Ca I.

Table 4. Features in the X-shooter spectra.

Feature	λ_{obs} (Å)	EW (Å)	EWc (Å)[a]
Al IIλ1671	∼3045	< 7.82	1.04 ± 0.02
Al IIIλ1855	∼3380	< 1.92	0.89 ± 0.02
Al IIIλ1863	∼3395	< 2.32	0.68 ± 0.02
Zn IIλ2026+Cr IIλ2026	∼3692	< 1.97	0.60 ± 0.02
Cr IIλ2062+Zn IIλ2063	∼3758	< 1.30	0.53 ± 0.02
Fe IIλ2261	∼4120	< 1.81	0.38 ± 0.02
Fe IIλ2344	∼4272	< 1.68	1.74 ± 0.02
Fe IIλ2374	∼4327	< 1.63	1.00 ± 0.02
Fe IIλ2383	∼4342	< 1.60	1.65 ± 0.02
Fe IIλ2587	4714.04	1.07 ± 0.47	1.33 ± 0.02
Fe IIλ2600	4737.32	2.47 ± 0.73	1.85 ± 0.03
Mg IIλ2796	5096.44	1.99 ± 0.34	1.71 ± 0.02
Mg IIλ2803	5109.09	1.50 ± 0.31	1.47 ± 0.02
Mg Iλ2853	5198.29	1.50 ± 0.40	0.78 ± 0.01
Ca IIλ3935	7171.01	0.72 ± 0.07	0.76 ± 0.02
Ca IIλ3970	7234.51	0.74 ± 0.07	0.66 ± 0.02
Ca Iλ4228	7705.26	0.37 ± 0.06	0.11 ± 0.02

Note. [a]Equivalents widths measured on the composite GRB afterglow spectrum (Christensen et al. 2011).

3.4 Modelling of the afterglow evolution

3.4.1 Model and fitting description

The afterglow emission was modelled with the numerical code of Jóhannesson et al. (2006). This software has been used successfully to model several different afterglows, including GRB 060121 (de Ugarte Postigo et al. 2006), GRB 050408 (de Ugarte Postigo et al. 2007), GRB 060526 (Thöne et al. 2010), and GRB 050525A (Resmi

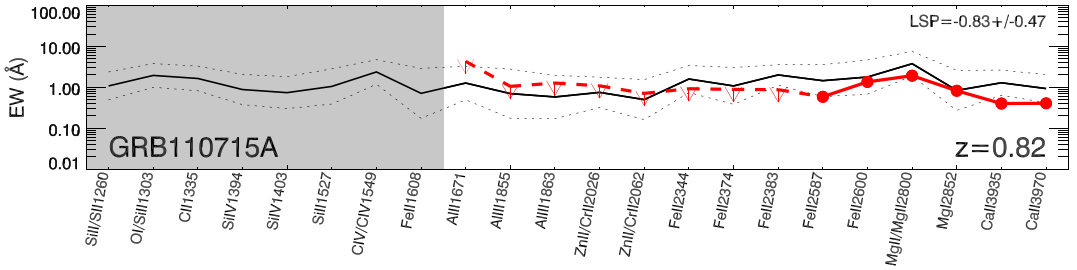

Figure 6. Line strength diagram of the afterglow spectrum of GRB 110715A, following the prescription of de Ugarte Postigo et al. (2012b).

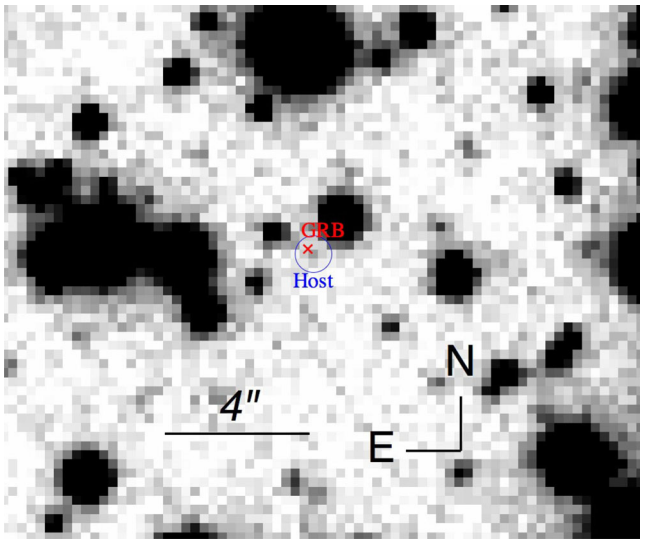

Figure 7. Observation of the host galaxy in the I_C-band from VLT/FORS2.

et al. 2012). This model assumes that the emission originates in a forward shock only, with a top-hat jet configuration. The algorithm simulates that a slab of matter with mass M_0 is ejected with a Lorentz factor of Γ_0 into a cone with a half-opening angle of θ_0. The slab starts accumulating matter and slows down in the process. Energy injections (E_i) at a time t_i are modelled as slabs of matter moving at lower speeds than the forward shock ($\Gamma_i < \Gamma_0$) and catching up to it at later times. At the time of collision, the energy and momentum of the forward shock of the injected slab are instantaneously added to the already moving mass. The emission from any RS formed in the collision is ignored. To calculate the emission, we assume that a fixed fraction of the energy of the forward shock is contained in the magnetic field and electron distribution of the forward shock. For the magnetic field, this fraction is denoted with ϵ_B. In Jóhannesson et al. (2006), the fraction of energy contained in the electrons was denoted with ϵ_e. This is now changed, to allow for the slope of the electron power-law distribution, p, to be less than 2. We used the formalism of Panaitescu & Kumar (2001) and denote with ϵ_i the fraction of energy contained in the electrons with the lowest energy in the distribution. The highest energy in the distribution is then limited such that the total energy of the electron distribution never exceeds a fraction ϵ_e of the forward shock energy.

To explain the data, we need a model that includes a temporary increase in flux around 0.3 d after the onset of the GRB that is observed in the light curves shown in Fig. 1. We chose three different types of models that we expect have this behaviour: a model with a constant density ISM (n_0) and a single energy injection (CM), a model with a wind density external medium ($\rho = A_* r^{-2}$) and a single energy injection (WM), and a model with a wind termination shock (with fractional change in density at the shock front denoted by r_{sh}) but no energy injection (TS).

Table 5. The lower and upper boundaries of the priors on parameters used in the analysis.

Parameter	Distribution	Lower	Upper
E_{iso} (10^{53} erg)	log-uniform	0.01	10 000
Γ_0	log-uniform	10	2000
θ_0 (deg)	log-uniform	0.1	90
p	uniform	1.1	4.0
ϵ_i	log-uniform	0.0001	0.5
ϵ_e	log-uniform	0.0001	0.5
ϵ_B	log-uniform	0.0001	0.5
A_* (5.015×10^{11} cm^{-3})	log-uniform	0.000 01	100
n_0 (cm^{-3})	log-uniform	0.0001	1000
t_{sh} (min)	log-uniform	0.000 01	200
r_{sh}	uniform	1	50
t_1^a (days)	log-uniform	0.0001	200
E_1/E_0^b	uniform	0	50
$A_{V,\,host}$ (mag)	uniform	0	1.0
$E(B-V)$ (mag)	Gaussian^c		

Notes. [a]t_1 is the time in the observer's frame at which the energy injection catches up with the forward shock.
[b]E_1 is the energy of the injection and E_0 is the initial energy release.
[c]$\mu = 0.56$ and $\sigma = 0.04$.

The best-fitting model parameters are found using Bayesian inference using the MULTINEST tool (Feroz, Hobson & Bridges 2009). MULTINEST is well suited for exploring the parameter space of the non-linear afterglow model and finds parameter correlation as well as all modes in the parameter space fitting the data similarly well. In addition to the afterglow model parameters, we also determine the host dust extinction in the fit, which we assume follows an SMC-like extinction curve. It is also possible to let the Galactic dust extinction vary as a nuisance parameter. This is of special interest in our case due to the large and uncertain value along the GRB line of sight through our Galaxy.

One of the main benefits of a Bayesian analysis is the introduction of prior distributions on parameters. For this analysis, we have unfortunately very little prior knowledge on their values. We therefore opted for flat priors on all parameters, but Galactic reddening, and made sure the parameter limits were large enough so that the posterior is not affected by these limits unless they are physical (see Table 5). Examples of such physical boundaries are the requirements that the extinction of the host be positive ($A_{V,host} > 0$) and the fractional change in density at the shock front should not decrease ($r_{sh} > 1$). We also constrain the fraction of energy in the electrons (ϵ_e) and magnetic field (ϵ_B) such that the fraction of energy contained in the rest of the jet, $\epsilon = 1 - \epsilon_e - \epsilon_B$, is larger than both

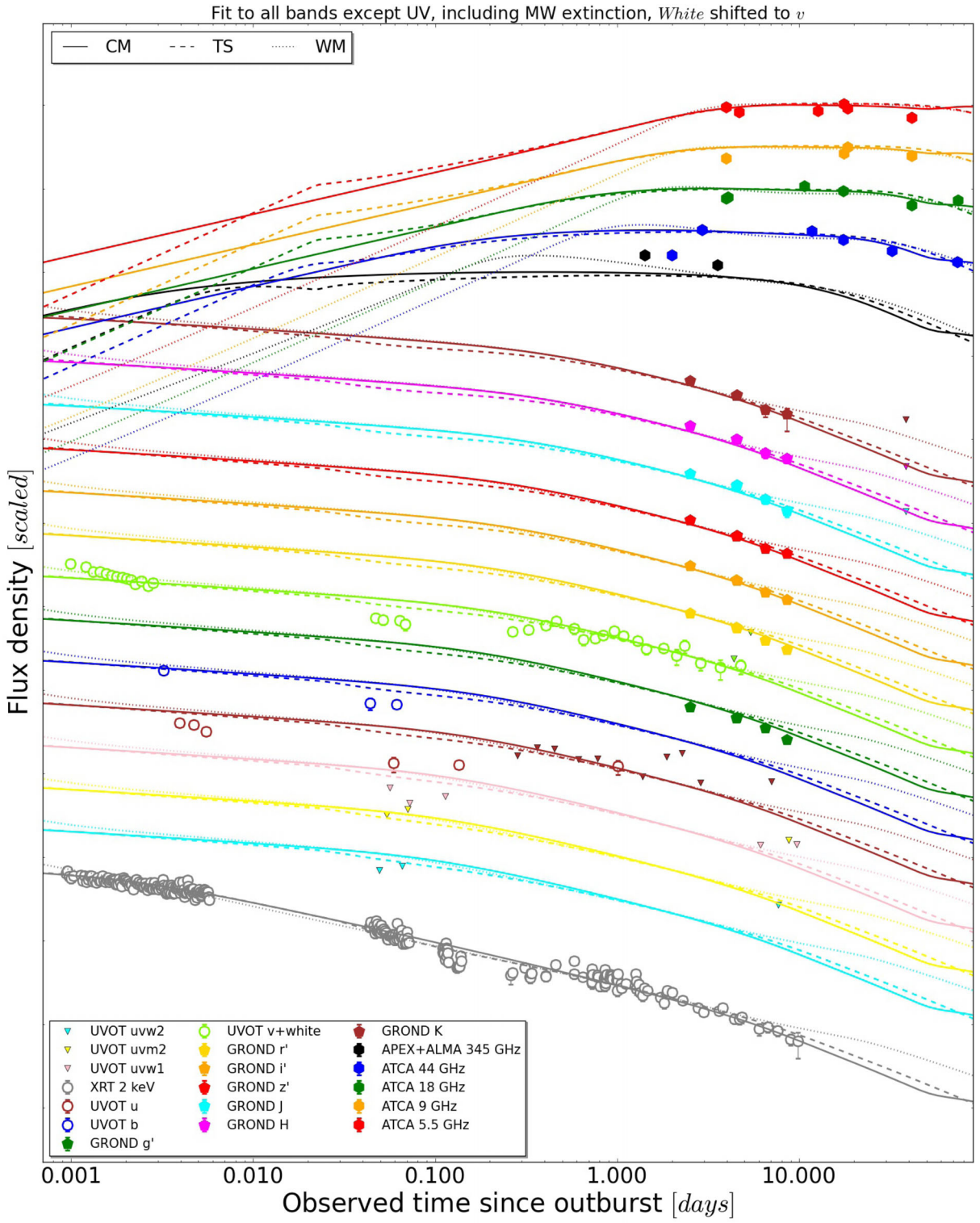

Figure 8. Best fits to the GRB 110715A light curves. Fluxes are independently scaled for each band for clarity. The full set of plots for each subset is available in the online version.

ϵ_e and ϵ_B. This is to make sure the jet's energy is not dominated by that of the electrons and the magnetic field. The constraint is not hard and ϵ is usually somewhere in between ϵ_e and ϵ_B if both are large like in this analysis. There is also the hard prior that $\epsilon_e > 1.1\epsilon_i$ so the energy in the total electron distribution is always at least 10 per cent greater than that contained in the electrons with the lowest value. This constraint is actually reached in all of our models, resulting in a strong correlation between ϵ_e and ϵ_i (see Fig. 12).

Due to several reasons, such as the high Galactic reddening, the wavelength range on which H I absorption is located, and the difficulties to compute the effective wavelength of the UVOT *white*

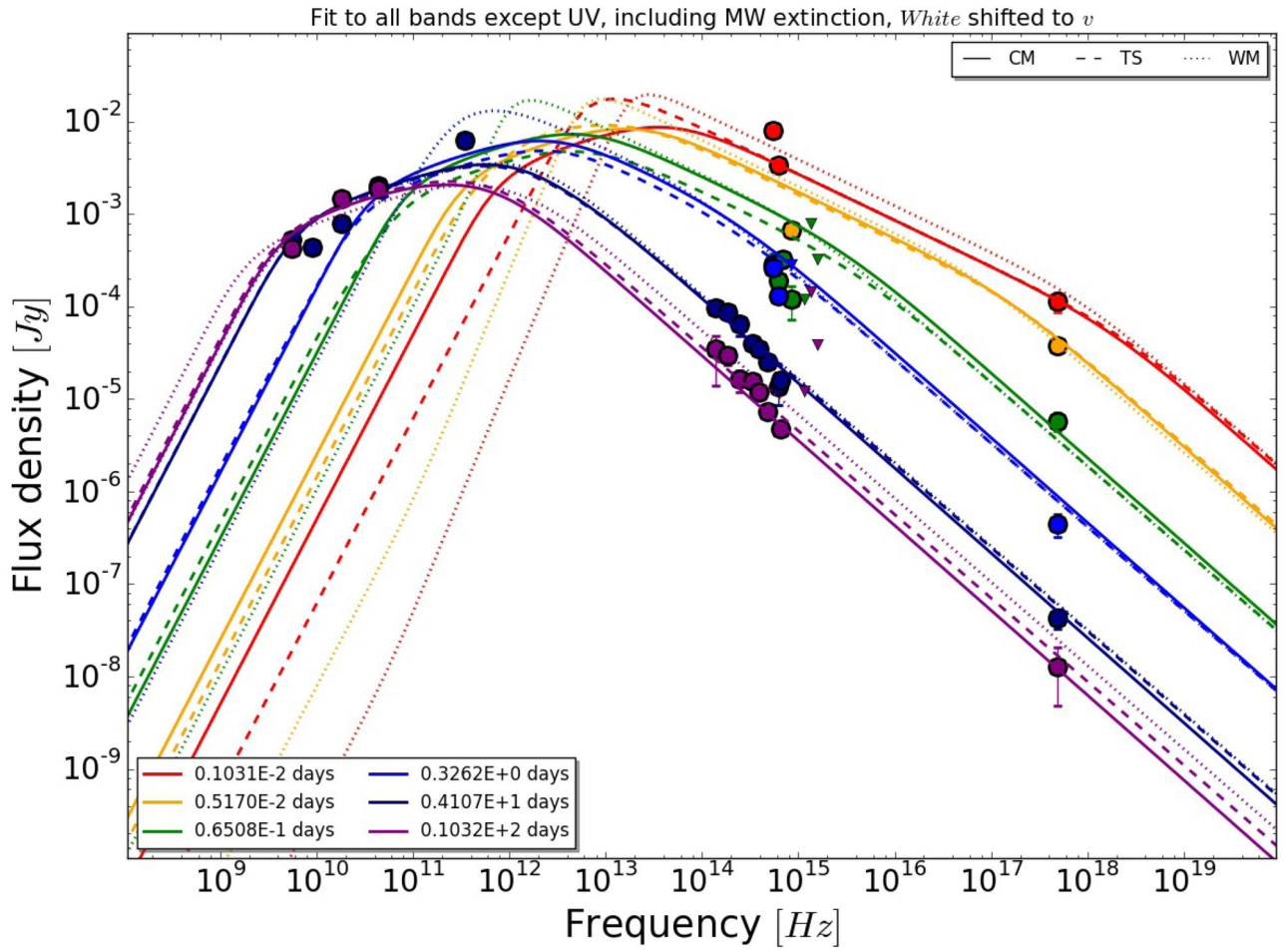

Figure 9. Best fits to the SED for GRB 110715A observed at several epochs. The full set of plots for each data subset is available in the online version.

filter due to its band width, we performed different fits in order to identify and quantify the sources of systematic uncertainties. We excluded the upper limits from the UV filters of UVOT as well as observations using its *u*-band filter because of the uncertainty on the Galactic dust extinction (none of the models are able to accurately reproduce those data points, either when included in the fit or not). Below we discuss the best-fitting results that were obtained, and refer the interested reader to the material contained in the Appendix A and online material for the result details of the complete set of Bayesian fits.

3.4.2 The best fit

We found the best-fitting models to be those in which we excluded the UV bands, we set MW extinction as a nuisance parameter, and the UVOT *white* band was shifted to V (see Table A1 for a detailed statistical analysis of the results for the complete grid of fits). This table suggests the TS fit as the most plausible model that describes the afterglow. However, none of them are either a statistically good fit or can fully explain the temporary flux increase at ∼0.3 d. We can also observe that there are no statistical arguments to reject most of the fits when compared with the best. Fit results are shown overlaid on the data in Figs 8 (light curves) and 9 (SEDs).

The time of the wind termination shock for the best TS model agrees very well with the time of the flux increase in the light curve. The density increases by a factor of 8.3 at that time, more than 2 times the expected density increase for strong shocks. Despite this, the effect on the light curves is not strong enough to explain the data. Due to the spectral parameters required in the fit, the wind termination shock causes a flux decrease rather than an increase as the cooling break is just below the optical band. The slow decay in the early X-ray light curve in the model is caused by the injection break being above the X-ray frequency. This requires there to be a spectral evolution in the X-ray light curve that is not observed. In both cases, the preferred location of the energy injection is at a different point than expected. For the best fit of the CM model, it is much later and serves only to explain the latest radio points while for the WM model it happens very early to explain the shallower decay between 0.01 and 1 d. The best model also has a hard time explaining the rapid decline in the light curve observed by the GROND instrument. The earliest points are underpredicted while the later points are overpredicted. This is again something that all the models fail to reproduce. The CM model does a slightly better job, but the WM model is worst. The models have a similarly hard time in explaining the late time X-ray light curve as they do not decay rapidly enough.

Fig. 10 compares the evolution of the photon index of our best-fitting models to that found from XRT data analysis. The CM and TS models do a reasonable job of explaining the X-ray spectral evolution with the exception of the first time bin where the models are harder than observed. The WM model agrees with the first time bin but is then too soft for the next two bins.

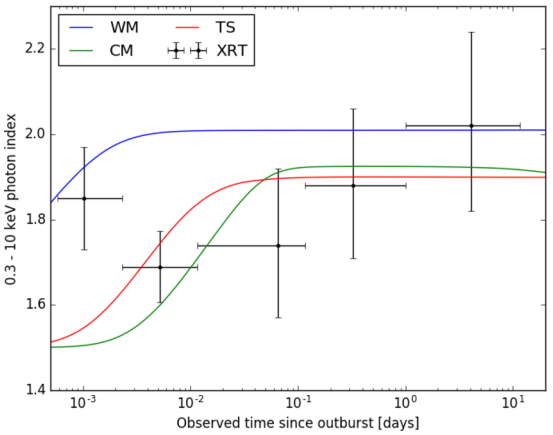

Figure 10. Best fit of the evolution of the photon index to that found from XRT data analysis. The full set of plots for each subset is available in the online version.

Finally, the best model is unable to explain the early and late radio and submillimetre data. The model has a hard time explaining the rapid rise of the 44 GHz data simultaneously with the decay of the 345 GHz data and the rather flat light curve at 5.5 GHz. The self-absorption break, ν_a, needs to pass through the 44 GHz band at around 2 d to explain the rapid increase and it should have already passed the 345 GHz band at 1 d and the 5.5 GHz band at 2 d. It is impossible for the model to meet these criteria. In addition, the 44 GHz light curve starts decaying at around 10 d with a slope that is incompatible with post jet-break evolution and at the same time the 18 GHz band is compatible with being nearly constant. The CM model has similar issues as the TS model although it does slightly better at late times because the injection lifts the radio light curve to match the last points. There is, however, no other indication for the energy injection and it is unlikely to be the correct physical interpretation. The WM model does the best job with the submillimetre and radio data, but is still far from explaining the details of the observed afterglow.

Table 6 shows the best-fitting model posterior median for the parameter values and their associated 68 per cent statistical errors. Fig. 11 shows a plot comparing the resulting distributions of the models for the best data subset. The parameter values that give the smallest χ^2 are usually located near the peak of the posterior distributions, and their distributions are mostly symmetric, with notable exceptions in the WM model where long tails can be seen for $E_{\rm iso}$, Γ_0, and θ_0. The inferred values are mostly typical for a GRB afterglow with a few exceptions. The half- opening angle θ_0 in the WM model is unreasonably low and requires an extreme confinement of the outflow. It is also the worst performer of the three models and we therefore consider it an unreasonable model. The value of the electron power-law index p is on the lower side and lower than expected from shock-acceleration theory (Achterberg et al. 2001). It is, however, well within the range of values deduced from observations of relativistic shocks (Shen, Kumar & Robinson 2006). The fraction of energy contained in the magnetic field and the electron distribution, ϵ_B, and ϵ_e, respectively, is rather large. ϵ_i is also larger than usual and constrained mostly by the equipartition requirements for the electron energy distribution rather than the position of the injection peak in the synchrotron spectrum. These

Table 6. The Bayesian evidence and the parameter posterior mean as reported by MULTINEST for the three different models of the best-fitting data set. The full table for each data subset is available in the online version.

Parameter	CM	TS	WM
Evidence	–1015.83	–995.70	–1129.24
χ^2_r	5.73	5.50	7.30
$\chi^{2\ a}_{r,x}$	2.47	2.15	2.76
$\chi^{2\ b}_{r,o}$	13.00	11.34	17.48
$\chi^{2\ c}_{r,r}$	26.79	32.54	36.38
$E_{\rm iso}$ (erg)	$53.63^{+0.66}_{-0.62} \times 10^{51}$	$55.10^{+0.92}_{-0.82} \times 10^{51}$	$0.38^{+0.60}_{-0.26} \times 10^{55}$
E_0 (erg)	$3.63^{+0.14}_{-0.12} \times 10^{50}$	$5.36^{+0.18}_{-0.17} \times 10^{50}$	$3.64^{+0.15}_{-0.14} \times 10^{49}$
Γ_0	1799^{+82}_{-110}	1510^{+180}_{-200}	184^{+35}_{-12}
θ_0 (deg)	$9.44^{+0.22}_{-0.20}$	11.32 ± 0.12	$0.35^{+0.27}_{-0.13}$
p	$1.8334^{+0.0038}_{-0.0036}$	1.8148 ± 0.0041	$1.8124^{+0.0037}_{-0.0039}$
ϵ_e	$9.32^{+0.57}_{-0.41} \times 10^{-2}$	$(11.64 \pm 0.40) \times 10^{-2}$	$(8.53 \pm 0.26) \times 10^{-2}$
ϵ_i	$(8.31 \pm 0.31) \times 10^{-2}$	$(10.44 \pm 0.32) \times 10^{-2}$	$(7.62 \pm 0.19) \times 10^{-2}$
ϵ_B	$(2.72 \pm 0.28) \times 10^{-1}$	$(1.59 \pm 0.16) \times 10^{-1}$	$(4.44 \pm 0.47) \times 10^{-2}$
A_* (5.015×10^{11} cm^{-3})	–	$0.01747^{+0.00078}_{-0.00074}$	$0.571^{+0.023}_{-0.022}$
n_0 (cm^{-3})	$1.05^{+0.12}_{-0.10}$	–	–
$t_{\rm sh}$ (min)	–	$3.13^{+0.13}_{-0.12} \times 10^1$	–
$r_{\rm sh}$	–	$8.33^{+0.56}_{-0.54}$	–
t_1 (days)	$5.03^{+0.42}_{-0.44} \times 10^1$	–	$(6.79 \pm 0.91) \times 10^{-4}$
E_1/E_0	$1.34^{+0.59}_{-0.35}$	–	$49.01^{+0.43}_{-0.61}$
$E_{\rm total}$ (erg)	$1.72^{+0.42}_{-0.24} \times 10^{51}$	$10.72^{+0.36}_{-0.34} \times 10^{50}$	$3.62^{+0.14}_{-0.12} \times 10^{51}$
$A_{V,\,\rm host}$ (mag)	$0.0048^{+0.0031}_{-0.0021}$	$0.0102^{+0.0063}_{-0.0046}$	$0.0099^{+0.0064}_{-0.0042}$
$E(B-V)$ (mag)	0.5249 ± 0.0030	$0.5277^{+0.0037}_{-0.0044}$	$0.5749^{+0.0035}_{-0.0043}$

Notes. [a] χ^2 computed only with the X-ray data.
[b] χ^2 computed only with the UV, optical and nIR data.
[c] χ^2 computed only with the submillimetre and millimetre data.

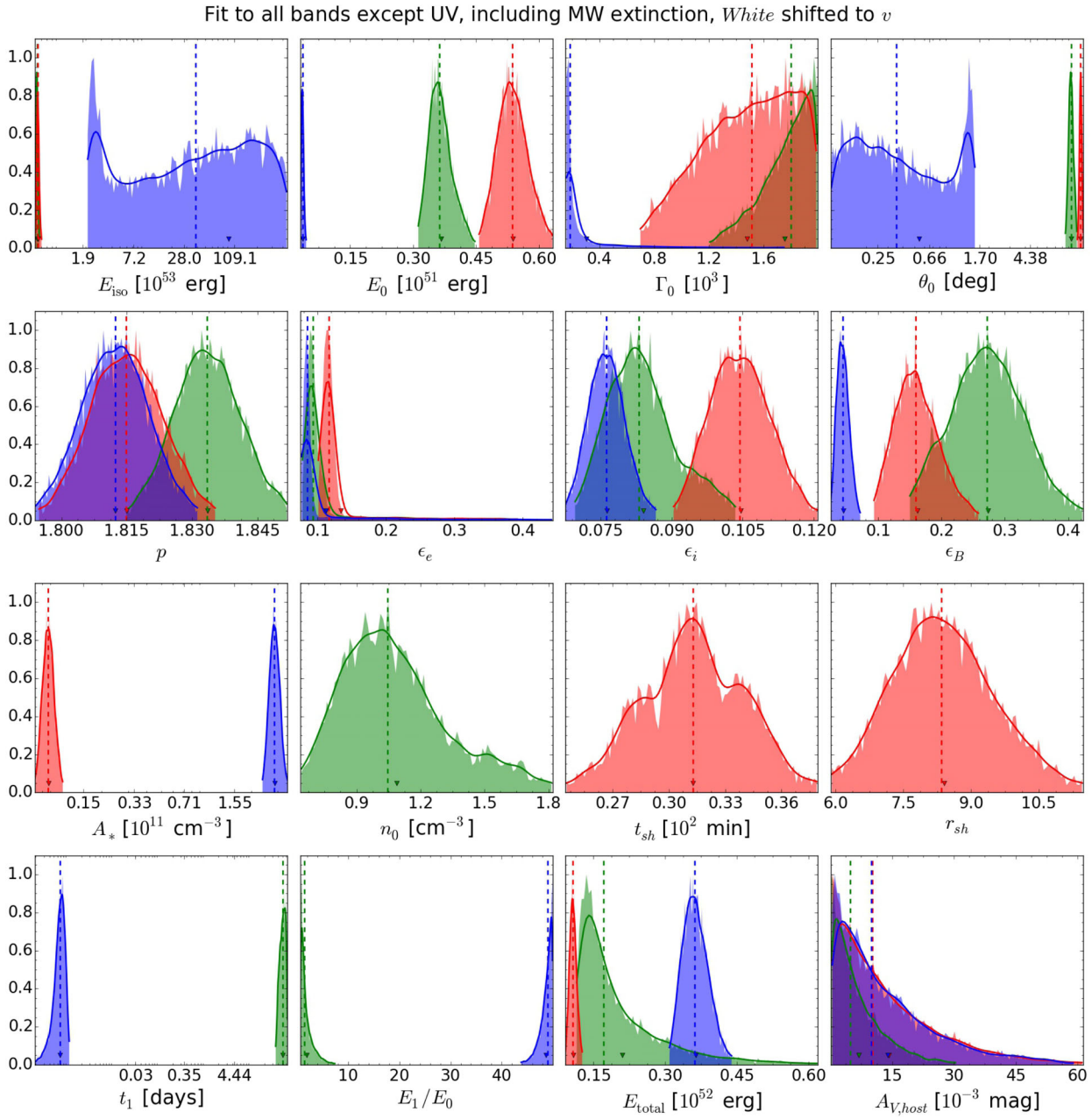

Figure 11. Posterior distributions of the three models for the best-fitting data subset. In all marginal plots, CM is represented in green, TS in red, and WM in blue. The full set of plots for each set is available in the online version.

large values cause the afterglow to be in the fast-cooling regime for the entire duration of the afterglow and the assumption of no radiative losses is likely invalid.

Our values for the host extinction are compatible with the value being very small as found earlier using GROND data only. The statistical error is significantly smaller because we use the entire data set, but the exact value is model dependent. As already discussed, the Galactic line-of-sight extinction is important in the GRB direction. The expected uncertainty could be large too, so similarly to the host galaxy, the Galactic $E(B-V)$ was left in some fits as a free parameter. Resulting Galactic and host-galaxy solutions show a clear anticorrelation, limiting our constraints of the inferred host galaxy $A_{V,\,\rm host}$. In Fig. 12, we include the two-dimensional marginal plots for the $E(B-V)$ of the Galactic extinction with the rest of the parameters when it is included in the fit. As shown in Appendix A, the galactic $E(B-V)$ value is model dependent, and results are somewhat bimodal, sometimes consistent with the dust maps of Schlegel et al. (1998), and sometimes with Schlafly & Finkbeiner (2011), the latter being the more favoured. The figures also show that the upper value found for the $E(B-V)$ parameter in this analysis is basically bound by the host extinction going to 0.

We also discuss in Appendix A the hypothesis that the RS contribution has to be taken into account (e.g. Jelínek et al. 2006; Laskar et al. 2013), as well as the possibility that a double jet model (e.g. Starling et al. 2005; Racusin et al. 2008; Filgas et al. 2011; van der Horst et al. 2014) is necessary to explain this afterglow. The conclusion is that, in spite of them possibly being present, none of the options can improve the fit starting at 0.5 d after the trigger, so

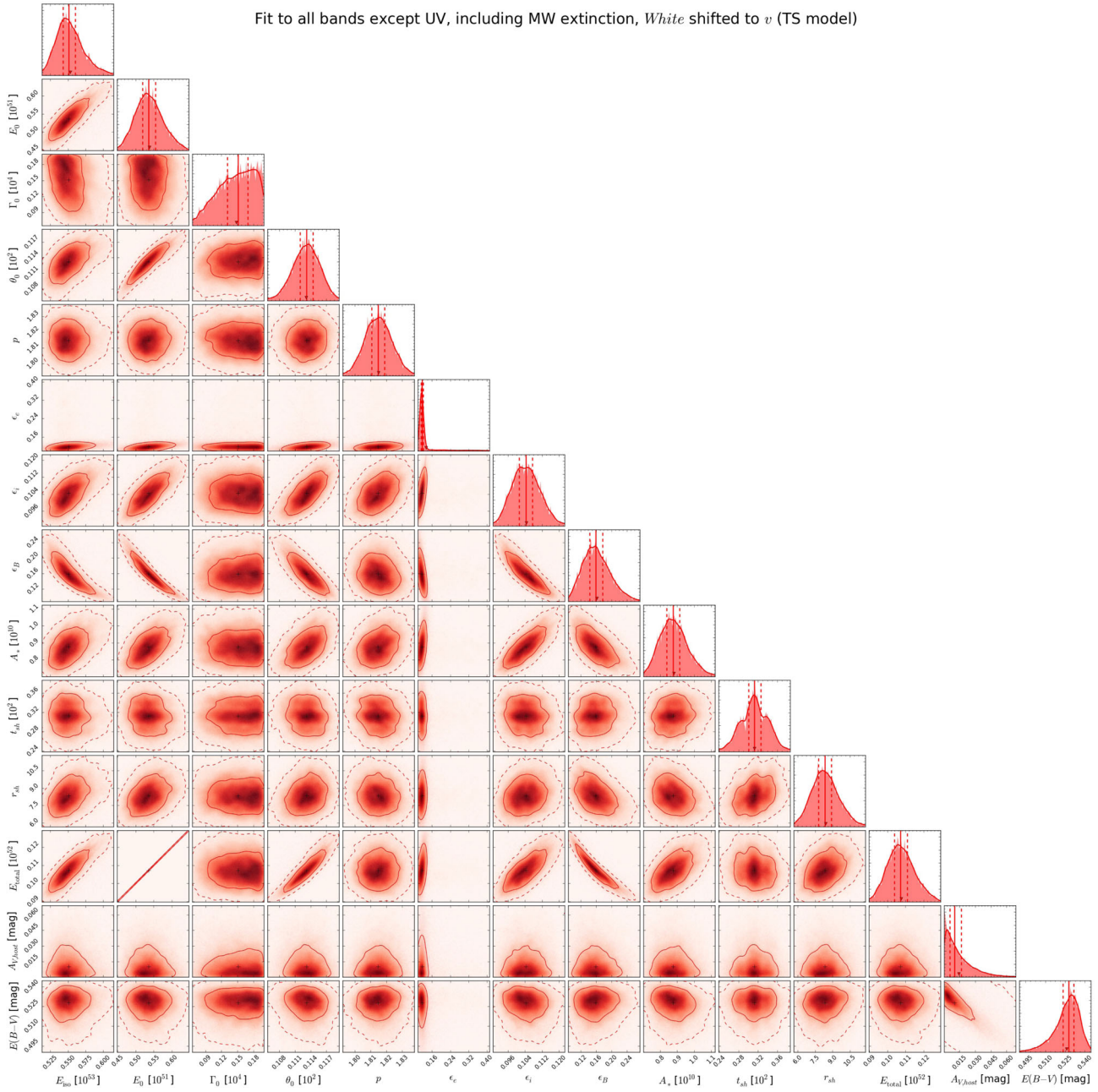

Figure 12. Parameter correlations for the best-fitting model. The full set of plots for each data subset is available in the online version.

other considerations must be taken into account to improve the fits we performed.

4 CONCLUSIONS

We present an extensive follow-up of the afterglow of GRB 110715A in 17 bands ranging from a few seconds up to 74 d after the trigger. The line of sight is affected by strong foreground Galactic extinction, which complicated the follow-up and the analysis of the data.

GRB 110715A had a very bright afterglow at all wavelengths, although its intrinsic luminosity is not exceptional.

Optical/nIR spectroscopy obtained with X-shooter shows weak absorption features at a redshift of $z = 0.8224$ with no resolved velocity components ($\lesssim$30 km s^{-1}). Absorption line ratios indicate a low-ionization environment, confirmed by the rare detection of Ca I.

Deep late imaging reveals a faint host galaxy with an absolute magnitude of $M_B = -18.2$. This is consistent with the weak absorption features detected in the spectrum.

We attempted to model the broad-band data with a fireball model based on the prescription of Jóhannesson et al. (2006). The best model implies a forward shock evolving through a wind environment with a termination shock. In spite of describing roughly the behaviour of the afterglow, none of the models are able to get a statistically acceptable fit. This shows the need for better broad-band sampling and more complex models to accurately describe the physics of GRB afterglows. There are several works that explore other possibilities, such as magneto-hydrodynamic simulations (van Eerten, van der Horst & MacFadyen 2012), which was satisfactorily

used, e.g. in Guidorzi et al. (2014); Ryan et al. (2015); Zhang et al. (2015), or central engine activities (Zhang et al. 2014). These and other effects might be considered together in future works to get a more accurate view of the GRB afterglow physics.

Radio and submillimetre, along with X-ray observations, have been proven to be the most constraining bands for the afterglow modelling. We were limited by sensitivity for a long time in the crucial wavelength range of submillimetre, but now that ALMA is available, we have a good chance of getting high-quality data for a larger number of GRBs. This new, current, and future facilities will allow us to probe the emission mechanisms in greater detail than previously possible, and will be determinant in the evolution of the GRB afterglow models.

ACKNOWLEDGEMENTS

In memory of Javier Gorosabel: an exceptional supervisor, a brilliant scientist, and an even better human being. RSR is grateful to SEPE for financial support while finishing this work and his PhD thesis. RSR, SRO, AJCT, YDH, SJ, and JCT acknowledge the financial support of the Spanish Government projects AYA 2009-14000-C03-01 and AYA 2012-39727-C03-01. Parts of this research were conducted by the Australian Research Council Centre of Excellence for All-sky Astrophysics (CAASTRO), through project No. CE110001020. AdUP and CT acknowledge support from Ramón y Cajal fellowships and from the Spanish research project AYA 2014-58381. JJ acknowledges financial contribution from the grant PRIN MIUR 2012 201278X4FL 002 'The Intergalactic Medium as a probe of the growth of cosmic structures'. DAK acknowledges the financial support by MPE Garching and TLS Tautenburg. Part of the funding for GROND (both hardware as well as personnel) was generously granted from the Leibniz-Prize to Prof. G. Hasinger (DFG grant HA 1850/28-1). PS and TK acknowledges support through the Sofja Kovalevskaja Award to P. Schady from the Alexander von Humboldt Foundation of Germany. AU is grateful for travel funding support through the Max-Planck Inst. for Extraterrestrial Physics. SK and ANG acknowledge support by DFG grant Kl 766/16-1. This work made use of data supplied by the UK Swift Science Data Centre at the University of Leicester.

Facilities: This publication is based on data acquired with the Atacama Pathfinder Experiment (APEX) under program 087.F-9301(A). This paper makes use of the following ALMA data: ADS/JAO.ALMA#2011.0.00001.E. ALMA is a partnership of ESO (representing its member states), NSF (USA) and NINS (Japan), together with NRC (Canada), NSC and ASIAA (Taiwan), and KASI (Republic of Korea), in cooperation with the Republic of Chile. The Joint ALMA Observatory is operated by ESO, AUI/NRAO and NAOJ. This publication is based on data acquired with the VLT/X-shooter under program 087.A-0055(C), as well as with VLT/FORS2 under program 091.A-0703(A).

REFERENCES

Achterberg A., Gallant Y. A., Kirk J. G., Guthmann A. W., 2001, MNRAS, 328, 393
Aihara H. et al., 2011, ApJS, 193, 29
Barthelmy S. D. et al., 2005, Space Sci. Rev., 120, 143
Bertin E., Arnouts S., 1996, A&AS, 117, 393
Bloom J. S., Kulkarni S. R., Djorgovski S. G., 2002, AJ, 123, 1111
Breeveld A. A., Landsman W., Holland S. T., Roming P., Kuin N. P. M., Page M. J., 2011, in AIP Conf. Proc. Vol. 1358, Gamma Ray Bursts 2010. Am. Inst. Phys., New York, p. 373
Burrows D. N. et al., 2005, Space Sci. Rev., 120, 165
Cano Z. et al., 2011, MNRAS, 413, 669
Castro-Tirado A. J. et al., 2001, A&A, 370, 398
Chandra P., Frail D. A., 2012, ApJ, 746, 156
Christensen L., Fynbo J. P. U., Prochaska J. X., Thöne C. C., de Ugarte Postigo A., Jakobsson P., 2011, ApJ, 727, 73
Crowther P. A., 2007, ARA&A, 45, 177
Cucchiara A. et al., 2011, ApJ, 736, 7
D'Elia V. et al., 2014, A&A, 564, A38
de Ugarte Postigo A. et al., 2006, ApJ, 648, L83
de Ugarte Postigo A. et al., 2007, A&A, 462, L57
de Ugarte Postigo A. et al., 2011, GRB Coordinates Network, 1216, 1
de Ugarte Postigo A. et al., 2012a, A&A, 538, A44
de Ugarte Postigo A. et al., 2012b, A&A, 548, A11
Evans P. A. et al., 2007, A&A, 469, 379
Evans P. A. et al., 2009, MNRAS, 397, 1177
Evans P. A. et al., 2010, A&A, 519, A102
Evans P. A., Goad M. R., Osborne J. P., Beardmore A. P., 2011, GRB Coordinates Network, 1216
Feroz F., Hobson M. P., Bridges M., 2009, MNRAS, 398, 1601
Filgas R. et al., 2011, A&A, 526, A113
Frail D. A., Kulkarni S. R., Nicastro L., Feroci M., Taylor G. B., 1997, Nature, 389, 261
Fynbo J. P. U. et al., 2009, ApJS, 185, 526
Galama T. J. et al., 1998, Nature, 395, 670
Gehrels N. et al., 2004, ApJ, 611, 1005
Goldoni P., Royer F., François P., Horrobin M., Blanc G., Vernet J., Modigliani A., Larsen J., 2006, in McLean I. S., Iye M., eds, Proc. SPIE Conf. Ser. Vol. 6269, Ground-based and Airborne Instrumentation for Astronomy. SPIE, Bellingham, p. 62692
Golenetskii S. et al., 2011, GRB Coordinates Network, 1216, 1
Greiner J. et al., 2008, PASP, 120, 405
Guidorzi C. et al., 2014, MNRAS, 438, 752
Hancock P. J., Murphy T., Schmidt B. P., 2011, GRB Coordinates Network, 1217
Hartoog O. E. et al., 2015, A&A, 580, A139
Hjorth J. et al., 2003, Nature, 423, 847
Horne K., 1986, PASP, 98, 609
Jelínek M. et al., 2006, A&A, 454, L119
Jóhannesson G., Björnsson G., Gudmundsson E. H., 2006, ApJ, 647, 1238
Johnston K. J., de Vegt C., 1986, in Proc. 19th IAU General Assembly Vol. 7, Highlights of Astronomy, p. 103
Kann D. A., Klose S., Zeh A., 2006, ApJ, 641, 993
Kann D. A. et al., 2010, ApJ, 720, 1513
Kann D. A. et al., 2011, ApJ, 734, 96
Kelson D. D., 2003, PASP, 115, 688
Kistler M. D., Yüksel H., Beacom J. F., Hopkins A. M., Wyithe J. S. B., 2009, ApJ, 705, L104
Klebesadel R. W., Strong I. B., Olson R. A., 1973, ApJ, 182, L85
Kopač D. et al., 2015, ApJ, 813, 1
Kouveliotou C., Meegan C. A., Fishman G. J., Bhat N. P., Briggs M. S., Koshut T. M., Paciesas W. S., Pendleton G. N., 1993, ApJ, 413, L101
Kovács A., 2008, in Duncan W. D., Holland W. S., Withington S., Zmuidzinas J., eds, Proc. SPIE Conf. Ser. Vol. 7020, Millimeter and Submillimeter Detectors and Instrumentation for Astronomy IV. SPIE, Bellingham, p. 702001
Krühler T. et al., 2008, ApJ, 685, 376
Krühler T. et al., 2015, A&A, 581, A125
Laskar T. et al., 2013, ApJ, 776, 119
Mészáros P., Rees M. J., 1993, ApJ, 405, 278
Modigliani A. et al., 2010, in Silva D. R., Peck A. B., Soifer B. T., eds, Proc. SPIE Conf. Ser. Vol. 7737, Observatory Operations: Strategies, Processes, and Systems III. SPIE, Bellingham. p. 773728
Mundell C. G. et al., 2013, Nature, 504, 119
Nelson P., 2011, GRB Coordinates Network, 1217
Oates S. R. et al., 2009, MNRAS, 395, 490
Panaitescu A., Kumar P., 2001, ApJ, 554, 667
Panaitescu A., Kumar P., 2002, ApJ, 571, 779

Perley D. A. et al., 2014, ApJ, 781, 37
Perley D. A. et al., 2016a, ApJ, 817, 7
Perley D. A. et al., 2016b, ApJ, 817, 8
Piranomonte S., Vergani S. D., Malesani D., Fynbo J. P. U., Wiersema K., Kaper L., 2011, GRB Coordinates Network, 1216
Planck Collaboration XVI, 2014, A&A, 571, A16
Racusin J. L. et al., 2008, Nature, 455, 183
Resmi L. et al., 2012, MNRAS, 427, 288
Rhoads J. E., 1997, ApJ, 487, L1
Robertson B. E., Ellis R. S., 2012, ApJ, 744, 95
Roming P. W. A. et al., 2005, Space Sci. Rev., 120, 95
Ryan G., van Eerten H., MacFadyen A., Zhang B.-B., 2015, ApJ, 799, 3
Salvaterra R. et al., 2009, Nature, 461, 1258
Sari R., Piran T., Narayan R., 1998, ApJ, 497, L17
Sari R., Piran T., Halpern J. P., 1999, ApJ, 519, L17
Sault R. J., Teuben P. J., Wright M. C. H., 1995, in Shaw R.A., Payne H.E., Hayes J.J.E., eds, ASP Conf. Ser. Vol. 77, Astronomical Data Analysis Software and Systems IV. Astron. Soc. Pac., San Francisco, p. 433
Schlafly E. F., Finkbeiner D. P., 2011, ApJ, 737, 103
Schlegel D. J., Finkbeiner D. P., Davis M., 1998, ApJ, 500, 525
Schulze S. et al., 2015, ApJ, 808, 73
Shen R., Kumar P., Robinson E. L., 2006, MNRAS, 371, 1441
Siringo G. et al., 2009, A&A, 497, 945
Skrutskie M. F. et al., 2006, AJ, 131, 1163
Sonbas E. et al., 2011, GRB Coordinates Network, 1215
Sparre M. et al., 2014, ApJ, 785, 150
Starling R. L. C., Wijers R. A. M. J., Hughes M. A., Tanvir N. R., Vreeswijk P. M., Rol E., Salamanca I., 2005, MNRAS, 360, 305
Tanvir N. R. et al., 2009, Nature, 461, 1254
Thöne C. C. et al., 2010, A&A, 523, A70
Tinney C. et al., 1998, IAU Circ., 6896, 1
Tody D., 1993, in Hanisch R. J., Brissenden R. J. V., Barnes J., ASP Conf, Ser. Vol. 52, Astronomical Data Analysis Software and Systems II. Astron. Soc. Pac., San Francisco, p. 173
Updike A. C., Schady P., Greiner J., Krühler T., Kann D. A., Klose S., Rossi A., 2011, GRB Coordinates Network, 1216
van der Horst A. J. et al., 2014, MNRAS, 444, 3151
van Dokkum P. G., 2001, PASP, 113, 1420
van Eerten H., van der Horst A., MacFadyen A., 2012, ApJ, 749, 44
Vergani S. D. et al., 2015, A&A, 581, A102
Vernet J. et al., 2011, A&A, 536, A105
Walker M. A., 1998, MNRAS, 294, 307
Wijers R. A. M. J., Galama T. J., 1999, ApJ, 523, 177
Wilson W. E. et al., 2011, MNRAS, 416, 832
Woosley S. E., Bloom J. S., 2006, ARA&A, 44, 507
Yoldaş A. K., Krühler T., Greiner J., Yoldaş A., Clemens C., Szokoly G., Primak N., Klose S., 2008, in AIP Conf. Proc, Gamma Ray bursts 2007: Proceedings of the Santa Fe Conference. Am. Inst. Phys., New York, p. 227
Zhang B., Yan H., 2011, ApJ, 726, 90
Zhang B.-B., Zhang B., Murase K., Connaughton V., Briggs M. S., 2014, ApJ, 787, 66
Zhang B.-B., van Eerten H., Burrows D. N., Ryan G. S., Evans P. A., Racusin J. L., Troja E., MacFadyen A., 2015, ApJ, 806, 15
Zheng W. et al., 2012, ApJ, 751, 90

SUPPORTING INFORMATION

Additional Supporting Information may be found in the online version of this article.

Table 1. Broad band multiwavelength observations of GRB110715A.
Figure 8. Best fits to the GRB 110715A light curves.
Figure 9. Best fits to the SED for GRB 110715A observed at several epochs.
Figure 10. Posterior distributions of the three models for the best-fitting data subset.
Figure 11. Parameter correlations for the best-fitting model.
Table 6. The Bayesian evidence and the parameter posterior mean as reported by MULTINEST for the three different models of the best-fitting data set.
Figure 12. Best fit of the evolution of the photon index to that found from XRT data analysis.
Table A1. The Bayesian evidence and reduced chi-square for all ($\chi^2_{\rm red}$), X-ray ($\chi^2_{{\rm red},x}$), optical ($\chi^2_{{\rm red},o}$), and radio ($\chi^2_{{\rm red},r}$) bands. (http://www.mnras.oxfordjournals.org/lookup/suppl/doi:10.1093/mnras/stw2608/-/DC1).

Please note: Oxford University Press is not responsible for the content or functionality of any supporting materials supplied by the authors. Any queries (other than missing material) should be directed to the corresponding author for the article.

APPENDIX A: GLOBAL VIEW OF ALL PERFORMED FITS

The goodness of the complete grid of fits is summarized in Table A1. This grid consists of different cuts in wavelength and time in order to get useful additional information that clarifies some details of the physical nature of the afterglow and systematic uncertainties.

To test the constraining power of each wavelength range, we split the data into three subsets: X-rays, [UV/]optical/nIR,[2] and submillimetre/millimetre. These were then fitted individually and also in sets of two.

We found that the optical light curves were best fit with the TS and WM model, where the early steep decay and the bump at around 0.3 d are easily explained. The TS model was slightly better, mostly due to a better fit to the early *white+v* band data. The TS model also does a better job of predicting the XRT and radio data while the WM model is orders of magnitude off. The CM model does not do as well with the optical data, a large energy injection in combination with a low value for p does a reasonable job in explaining the late light curves, but the early *white+v* band data are not explained. The CM model also fares better with predicting the XRT and radio/submillimetre data, although it is obviously not able to reproduce them completely.

The fit to the radio data is less discriminating, the WM models are better than both the TS and CM models, but only marginally. The parameters for the WM and TS models are very similar and the energy injection and wind termination shock both happen at late times to improve the fit to the late radio points. The CM model stands out from the group with the energy injection happening at early times and is therefore the worst offender at late times. The CM model, however, is best at predicting the optical and X-ray data and roughly goes through the late time optical/nIR curves and the XRT curves. The WM and TS model under-predict those same data, with the WM model being the worst offender. Early observations would helped in constraining the better modelled light curves.

No attempt was made at fitting the XRT light curve only, but when we add it to the mix with either the optical/NIR or the radio/submillimetre data things change considerably. For the former set it is now the TS model that is best, trailed by the CM and then the WM model. None of the models now explain the bump in the optical light curves, but at least the TS model explains the wiggles

[2] We include in the UV UVOT filters uvw1, uvw2, uvm2, and u.

Table A1. The Bayesian evidence and reduced chi-square for all ($\chi^2_{\rm red}$), X-ray ($\chi^2_{{\rm red},x}$), optical ($\chi^2_{{\rm red},o}$), and radio ($\chi^2_{{\rm red},r}$) bands. A detailed table for each model is available in the online version.

Fit Id	Evidence	$\chi^2_{\rm red}$	$\chi^2_{{\rm red},x}$	$\chi^2_{{\rm red},o}$	$\chi^2_{{\rm red},r}$
CM/XOR/WC	− 1066.52 ± 0.19	6.52	2.45	16.49	27.98
TS/XOR/WC	− 951.65 ± 0.20	6.24	2.0	16.12	30.48
WM/XOR/WC	− 1181.09 ± 0.19	9.78	2.61	29.6	39.61
CM/XUOR/WN	− 1677.46 ± 0.20	6.92	2.46	15.75	35.57
TS/XUOR/WN	− 1503.57 ± 0.20	6.79	1.92	18.22	31.42
WM/XUOR/WN	− 1753.24 ± 0.20	57.02	2.25	259.83	47.46
CM/XOR/WN	− 1667.78 ± 0.20	6.79	2.45	15.86	35.35
TS/XOR/WN	− 1491.05 ± 0.20	6.5	1.91	17.61	31.27
WM/XOR/WN	− 1730.71 ± 0.20	54.46	2.21	261.71	47.0
CM/XOR/VC	− 1039.59 ± 0.20	5.69	2.49	12.62	26.91
TS/XOR/VC	− 988.59 ± 0.20	5.51	2.14	11.86	31.2
WM/XOR/VC	− 1145.41 ± 0.19	7.45	2.73	18.03	37.6
CM/XOR/VN	− 1015.83 ± 0.21	5.73	2.47	13.0	26.79
TS/XOR/VN	− 995.70 ± 0.20	5.5	2.15	11.34	32.54
WM/XOR/VN	− 1129.24 ± 0.19	7.3	2.76	17.48	36.38
CM/O/VC	− 201.49 ± 0.16	175.87	8.82	37.34	2997.26
TS/O/VC	− 206.60 ± 0.18	71.38	19.67	70.76	800.15
WM/O/VC	− 237.56 ± 0.15	727.47	277.16	228.39	8762.93
CM/R	− 267.53 ± 0.16	57.98	48.6	100.81	25.24
TS/R	− 252.66 ± 0.15	195.24	135.6	457.94	23.98
WM/R	− 249.27 ± 0.18	467.74	190.45	1597.79	22.54
CM/XUO/VC	− 555.22 ± 0.18	164.1	1.88	13.01	3000.39
TS/XUO/VC	− 466.51 ± 0.21	53.66	1.73	68.71	727.94
WM/XUO/VC	− 733.27 ± 0.18	183.79	2.12	14.73	3359.54
CM/XR/	− 600.80 ± 0.18	8.4	2.38	25.9	25.76
TS/XR/	− 558.08 ± 0.18	8.82	1.87	29.13	28.49
WM/XR/	− 671.99 ± 0.18	10.69	2.29	35.22	34.55
CM/UOR/VC	− 561.73 ± 0.19	20.83	18.66	26.5	30.35
TS/UOR/VC	− 541.22 ± 0.19	47.79	41.7	77.02	25.68
WM/UOR/VC	− 676.66 ± 0.19	23.52	25.91	11.13	35.58
CM/XUOR/VCE	− 848.73 ± 0.19	9.82	3.66	21.3	28.05
TS/XUOR/VCE	− 670.00 ± 0.20	13.16	2.24	39.29	29.35
WM/XUOR/VCE	− 1044.04 ± 0.19	15.01	3.05	38.75	46.29
CM/XUOR/VCL	− 547.08 ± 0.18	14.02	1.65	26.9	28.55
TS/XUOR/VCL	− 494.77 ± 0.19	20.93	1.86	47.0	29.91
WM/XUOR/VCL	− 672.83 ± 0.18	65.64	2.99	174.44	45.23

Notes. Fit Id = (A)/(B)/(C)(D)(E)
(A) = Model used (CM/TS/WM).
(B) = Wavelength range of the observations used for the model fitting:
X = XRT 2 keV
U = UVOT UVW2, UVM2, UVW1, and U
O = Rest of the UVOT and GROND bands
R = Radio and sub-mm bands
(C) = UVOT *white* band shifted to UVOT (V) or independent (W).
(D) = Treatment of the Galactic reddening:
C = Corrected
N = Set to a nuisance parameter
(E) = Time interval used for the model fitting:
E = From $t = 0.05$ d
L = From $t = 0.5$ d

in the XRT light curve. The early *white+v* optical data are also not explained. In this case, the TS and WM models do a fairly good job of predicting the radio/submillimetre data, but the CM model is way off. For the latter set of XRT and radio/submillimetre, we get a pretty consistent picture of the three models. The TS model is best, trailed by the CM model and finally the WM model like for the entire set. The resulting parameter distributions are actually fairly close to the results of the entire data set, indicating that the additional information from the optical data does not constrain the model much. All of the models actually predict the optical data reasonably well and the full fit gives only small visible changes. This means that the large spectral lever arm added to the very fine temporal sampling of the XRT light curves is most constraining for the model.

Our final combination is the UV/radio/submillimetre and optical/NIR data together. Here the CM model shows the best fit, which fairs similarly to the WM, and significantly better fit than TS model. None of them are able to explain the bump in optical, but the early optical and early radio/submillimetre data are well explained by the TS model. All of the models approximately predict

the XRT light curve but with some offset in the temporal behaviour. There is therefore little additional constraining power in the spectral information from the XRT data, but mostly from the very detailed time behaviour.

In conclusion, it seems that the fine sampling in the XRT light curve with the large spectral lever arm of the radio and submillimetre data is the most constraining data for the models. We also note that the inferred physical conditions can vary up to few orders of magnitude depending on the model and the wavelength ranges considered. Therefore, observational sampling is fundamental in order to discriminate different models and constrain its physical parameters.

To reduce the bias from the early UVOT *white+v* band points that can be caused by a RS (e.g. Jelínek et al. 2006), we redo the analysis with all optical points before 0.005 d turned into upper limits. We note that a RS can also contribute at later times in submillimetre and millimetre bands, (e.g. Laskar et al. 2013; Perley et al. 2014). However, it is not needed to include them for the qualitative overview we want to give. The parameters of the models are mostly unchanged with this exclusions of the data. A notable exception is the values of ϵ_e, ϵ_i, and ϵ_B. ϵ_B is reduced significantly while both ϵ_e and ϵ_i increase. This affects the determined host extinction which is now determined to be twice as large. The models are still unable to reproduce the data and most of the comments still apply. The contribution of a RS may help to explain the early evolution in the *white* filter and the early submillimetre (and maybe mm) light curves, but will not help with the rest of the data. Thus, the early *white* band data are not the driving cause for the models not being able to reproduce the bump.

One possibility that has often been proposed to model complex GRB light curves is the double jet model (e.g. Starling et al. 2005; Racusin et al. 2008; Filgas et al. 2011; van der Horst et al. 2014), the early light curve being dominated by a fast moving narrow jet while a slow moving wide jet dominates at late time. This can be considered the simplest model for a two-dimensional jet. To test if this is the case here, we fit the data after 0.5 d only, turning all other points into upper limits. The TS model is still the best model in this case and it is mostly able to explain the optical and X-ray bump at 0.3 d, but all the other considerations still apply and the radio/submillimetre data are still poorly modelled. We therefore conclude that a double jet model is not appropriate for this case.

[1]*Instituto de Astrofísica de Andalucía (IAA-CSIC), Glorieta de la Astronomía s/n, E-18008 Granada, Spain*
[2]*Unidad Asociada Grupo Ciencias Planetarias (UPV/EHU, IAA-CSIC), Departamento de Física Aplicada I, E.T.S. Ingeniería, Universidad del País Vasco (UPV/EHU), Alameda de Urquijo s/n, E-48013 Bilbao, Spain*
[3]*Ikerbasque, Basque Foundation for Science, Alameda de Urquijo 36-5, E-48008 Bilbao, Spain*
[4]*Sydney Institute for Astronomy, School of Physics, The University of Sydney, NSW 2006, Australia*
[5]*ARC Centre of Excellence for All-sky Astrophysics (CAASTRO), Australia*
[6]*Science Institute, University of Iceland, IS-107 Reykjavik, Iceland*
[7]*Dark Cosmology Centre, Niels Bohr Institute, Juliane Maries Vej 30, DK-2100 Copenhagen, Denmark*
[8]*Thüringer Landessternwarte Tautenburg, Sternwarte 5, D-07778 Tautenburg, Germany*
[9]*Max-Planck-Institut für extraterrestrische Physik, Giessenbachstraße 1, D-85748 Garching, Germany*
[10]*European Southern Observatory, Alonso de Córdova 3107, Vitacura, Santiago, Chile*
[11]*Mullard Space Science Laboratory, University College London, Holmbury St. Mary, Dorking, Surrey RH5 6NT, UK*
[12]*INAF – Osservatorio Astronomico di Trieste, via G. B. Tiepolo 11, I-34131 Trieste, Italy*
[13]*Joint ALMA Observatory, Alonso de Córdova 3107, Vitacura, Santiago, Chile*
[14]*INAF-Osservatorio Astronomico di Roma, via Frascati 33, I-00040 Monte Porzio Catone (RM), Italy*
[15]*ASI-Science Data Center, Via del Politecnico snc, I-00133 Rome, Italy*
[16]*APC, Univ. Paris Diderot, CNRS/IN2P3, CEA/Irfu, Obs. de Paris, Sorbonne Paris Cit, France*
[17]*Universe Cluster, Technische Universität München, Boltzmannstraße 2, D-85748 Garching, Germany*
[18]*Astronomical Institute of the Czech Academy of Sciences, Fričova 298, CZ-25165 Ondřejov, Czech Republic*
[19]*Institute of Science and Technology in Space, SungKyunKwan University, Suwon 16419, Republic of Korea*
[20]*Harvard-Smithsonian Center for Astrophysics, 60 Garden St., Cambridge, MA 02138, USA*
[21]*European Space Astronomy Center, ISDEFE, ESA, Villafranca del Castillo, 50727, E-28080 Madrid, Spain*
[22]*INAF-IASF Bologna, Area della Ricerca CNR, via Gobetti 101, I-40129 Bologna, Italy*
[23]*Astrophysics Data System, Harvard-Smithonian Center for Astrophysics, Garden St. 60, Cambridge, MA 02138, USA*
[24]*Department of Chemistry and Physics, Roger Williams University, One Old Ferry Road, Bristol, RI 02809, USA*
[25]*Department of Physics and Astronomy, University of Leicester, University Road, Leicester LE1 7RH, UK*
[26]*Scientist Support LLC, Madison, AL 35758, USA*

This paper has been typeset from a TEX/LATEX file prepared by the author.